International Journal of Multiphase Flow 167 (2023) 104520

Contents lists available at ScienceDirect

International Journal of Multiphase Flow

journal homepage: www.elsevier.com/locate/ijmulflow

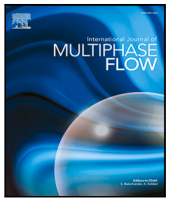

A computational study of a two-fluid atomizing coaxial jet: Validation against experimental back-lit imaging and radiography and the influence of gas velocity and contact line model

Lam Vu [a,*], Nathanaël Machicoane [b,d], Danyu Li [c], Timothy B. Morgan [c], Theodore J. Heindel [c], Alberto Aliseda [b], Olivier Desjardins [a]

[a] Department of Mechanical and Aerospace Engineering, Cornell University, Ithaca, USA
[b] Department of Mechanical Engineering, University of Washington, Seattle, USA
[c] Center for Multiphase Flow Research and Education and Department of Mechanical Engineering, Iowa State University, Ames, USA
[d] Univ. Grenoble Alpes, CNRS, Grenoble INP, LEGI, 38000 Grenoble, France

ARTICLE INFO

Keywords:
Air-blast atomization
Contact line modeling
Liquid–gas flows
Validation

ABSTRACT

Numerical simulations of liquid atomization in a two-fluid coaxial geometry have been performed using a geometric Volume-of-Fluid method. Experimental measurements have been obtained using visible light back-lit imaging and X-ray radiography. Simulations are validated against experiments, using the same geometry and fluid injection rates of air and water, by showing excellent agreement in quantities such as liquid mass distribution in the spray formation region and the liquid jet length statistics and temporal dynamics. At the nozzle exit, the coflowing liquid and gas streams are separated by a cylindrical splitter plate. The liquid is laminar and modeled using a Poiseuille flow while the gas inflow model and the contact line model are varied. For the gas velocity models, the vorticity thickness is shown to have a strong influence on the downstream liquid distribution; the difficulty of its modeling and routes to overcome them are discussed. For the contact line model, pinning the interface to the inner wall of the splitter plate leads to an initial increase in the diameter of the liquid jet just downstream of the nozzle exit. In contrast, pinning to the outer wall of the splitter plate or allowing for a free moving contact line results in a monotonic decrease in the diameter of the liquid jet as the downstream distance is increased, in agreement with the experimental observations and measurements. A sub-grid scale contact line model based on a static contact angle is introduced. The static contact angle is varied in the model, showing that the liquid remains intact longer as the static contact angle is increased.

1. Introduction

Two-fluid coaxial atomizers utilize a high-speed gas stream to destabilize a coflowing low-speed liquid jet. These devices are widely used in engineering systems such as spray dryers and fuel injectors. Accurate modeling of the liquid jet's initial destabilization and break up is of the upmost importance as it serves as an initial condition for the spray dispersion process. Because of the inherent difficulties associated with modeling primary atomization computationally (Gorokhovski and Herrmann, 2008), studies have mostly been limited to highly simplified and academic cases. Moreover, few studies have explored in detail the modeling of the nozzle exit. In particular, the impact of different modeling strategies for the high-speed gas, low-speed liquid, and the splitter plate separating the two streams, warrants careful investigation.

Liquid atomization has been studied extensively both through experiments and simulations but have had limitations based on the methods used. A non-exhaustive list of such methods are described below along with some of their limitations. Experimentally, the flow inside the nozzle cannot be easily quantified using standard particle image velocimetry (PIV) and hot-wire measurements. Back-lit imaging is an effective technique for visualizing the spray and can be used to accurately extract quantitative measurements of the liquid presence in a region where the liquid stays mostly intact (Machicoane et al., 2020). However, such measurements struggle in areas where the liquid is broken up and multiple liquid structures intersect a line of sight. In contrast, X-ray radiography penetrates the liquid, enabling the study of additional physics, such as bubble entrainment and contact line dynamics in extreme atomization conditions (Machicoane et al., 2019).

* Corresponding author.
E-mail address: lxv2@cornell.edu (L. Vu).

https://doi.org/10.1016/j.ijmultiphaseflow.2023.104520
Received 15 December 2022; Received in revised form 15 March 2023; Accepted 16 May 2023
Available online 25 May 2023
0301-9322/Published by Elsevier Ltd.

Recently, it has been used to extract quantitative measurements such as the integrated liquid depth along a line of sight (Bothell et al., 2020). Simulations have had their own challenges such as robust numerical methods capable of handling topology change, discontinuous fluid properties across the interface and singular forces at the interface, and computational demand owing to the wide range of length and time scales (Gorokhovski and Herrmann, 2008). Front tracking methods (Tryggvason et al., 2001), which transport a surface mesh, are viable techniques but have difficulty with topology change as heuristics are needed for the deletion and re-population of surface elements. Diffuse interface methods (Anderson et al., 1998) are also viable techniques, but diminish the sharpness of the discontinuities since the interface is smeared over a few computational cells. Level-set methods, which transport a signed distance function away from the interface, have been used extensively (Sethian and Smereka, 2003) but suffer from mass conservation issues. These issues have been addressed by improvements such as the conservative level-set method (Chiodi and Desjardins, 2017) and the refined grid level-set method (Hermann, 2008). Volume-of-Fluid (VOF) methods, using complex geometric transport operations (Owkes and Desjardins, 2014), have had success in handling topology change, ensuring discrete mass conservation and maintaining the sharp discontinuities.

Validating simulations against experiments is a crucial step in computational studies of sprays and the majority of past validation exercises of two-fluid atomizers have compared indirect quantities or reduced the modeling complexity because of the computational and experimental challenges described above. Demoulin et al. (2007) simulated primary break up by solving equations for a single fluid representing a liquid–gas mixture under the assumptions of high Reynolds and Weber numbers and compared centerline liquid volume fraction profiles against experiments. Gorokhovski and Herrmann (2008) modeled the primary atomization by solving for the gas phase using a large-eddy simulation (LES) and the liquid phase using a stochastic liquid depletion modeling. This study yielded satisfactory agreement of liquid volume fraction distributions against experiments but most comparisons were qualitative. Fuster et al. (2009) presented simulations in a planar configuration at a lower viscosity and density ratio and compared droplet size distributions, as a function of mesh size, against experimental data. Fuster et al. (2013) studied the influence of the splitter plate thickness on the peak frequency and made comparisons against linear stability analysis at low density ratios. For a single case, the frequency was compared against experiments and linear stability analysis at air–water conditions. The study showed that at low gas-to-liquid dynamic pressure ratios, a convective instability is observed whereas at high dynamic pressure ratios, the instability is absolute. Xiao et al. (2014) simulated primary atomization at air–water conditions and showed great agreement in the average liquid core length, where the liquid core is defined to be the large coherent liquid structure attached to the nozzle, but generated the gas inflow using synthetic turbulence. This study showed the turbulent eddies in the liquid phase play a leading role on the interfacial instabilities. Müller et al. (2016) simulated primary break up of a high-viscosity fluid and showed excellent agreement in liquid core length and dominant frequency against experiments using the same geometry. Agbaglah et al. (2017) presented 3D simulations in a planar geometry at experimental air–water conditions and compared well the liquid cone length and the most unstable frequency. This study showed that inclining the gas inflow enhanced the formation of interfacial waves. Ling et al. (2017) performed massively resolved simulations at a lower density and viscosity ratio and reported on droplet size distributions, as a function of mesh size, and compared them against log-normal and Gamma distribution fits. The simulations qualitatively discussed the expansion of punctured holes in liquid sheets and the ligaments generated at the edge of their rims. Carmona et al. (2021) performed simulations of a pre-filmed air-blast atomizer and made qualitative comparisons and drop size comparisons as a function of VOF iso-surface value. Even with current studies, more detailed and direct comparisons under realistic configurations are needed to validate computational capabilities.

In this work, we perform simulations of primary atomization in a coaxial two-fluid atomizer using the Volume-of-Fluid method and validate them against experiments. A novelty of our validation exercise is that we make direct comparisons of quantities obtained from experimental back-lit imaging and X-ray radiography under identical operating conditions, using the same geometry. Furthermore, the validation is comprehensive, including comparisons of liquid mass distribution and temporal dynamics of the liquid jet. Following the validation, we study the effect of using different gas inflow models which range from using an analytical velocity profile to a nozzle simulation. The liquid is laminar and modeled as a Poiseuille flow and a cylindrical splitter plate separates the liquid and gas streams. We discuss the influence of the contact line model which ranges from pinning the interface to a specified location on the splitter plate (fixed triple point) to a free moving contact line. For free moving contact lines, we employ a sub-grid scale (SGS) contact line model that assumes a static contact angle (Wang and Desjardins, 2018). We vary the static contact angle to understand the effect of nozzle tip wettability. These inflow modeling strategies are easily implementable and do not require large amounts of mesh resolution, making them particularly desirable from a practical engineering standpoint.

The paper is organized as follows: Section 2 discusses the experimental and numerical methods used, Section 3 validates our computational model against experiment, Section 4 discusses the influence of the gas velocity model, Section 5 discusses the influence of the contact line model, and conclusions are drawn in Section 6.

2. Methods

2.1. A canonical atomizer and flow conditions

Fig. 1 shows the two-fluid coaxial atomizer (Machicoane et al., 2019) used in both simulations and experiment. Air enters the nozzle through four upstream ports perpendicular to the wall and flows through an annular passage at a total flow rate Q_g. Liquid water flows through a straight circular pipe at a flow rate Q_l. The outer wall of the liquid nozzle separates the two streams and its annular section at the exit plane, with inner and outer nominal diameter $d_l = 2$ mm and $D_l = 3$ mm, will be referred to as the splitter plate. The liquid and gas bulk exit velocities are defined as $U_l = Q_l/A_l$ and $U_g = Q_g/A_g$, where $A_l = \pi d_l^2/4$ and $A_g = \pi(d_g^2 - D_l^2)/4$ are the liquid and gas nozzle exit flow-through areas and $d_g = 10$ mm is the gas nozzle inner diameter. The fluid properties used are kinematic viscosities of $\nu_g = 1.45 \times 10^{-5}$ m^2 s^{-1} and $\nu_l = 1.137 \times 10^{-6}$ m^2 s^{-1}, densities of $\rho_g = 1.226$ kg m^{-3} and $\rho_l = 1000$ kg m^{-3}, and a surface tension coefficient $\sigma = 72$ mN m^{-1} where subscripts g and l denote gas and liquid properties respectively. Table 1 summarizes the non-dimensional parameters used in this case.

2.2. High-speed back-lit imaging and X-ray radiography

High-speed back-lit imaging is used to produce 2D projections of the liquid presence in the near-field. The images are post-processed using a sequence of operations that binarize the liquid core, defined to be the portion of the liquid jet that is still fully connected to the nozzle, such that a liquid pixel value is 1 and a gas pixel value is 0. The temporal and spatial resolutions for this study are 0.1 ms and 27 μm respectively. Details of this method are discussed further in Machicoane et al. (2020).

Synchrotron X-ray radiography of the resulting spray was performed at the Advance Photon Source (APS) at Argonne National Laboratory, 7-BM beamline (Kastengren et al., 2012). As opposed to binarized liquid data obtained from back-lit imaging, focused-beam radiography enables the point-wise measurement of the integrated liquid depth along a line of sight, referred to as the equivalent path length (EPL). The

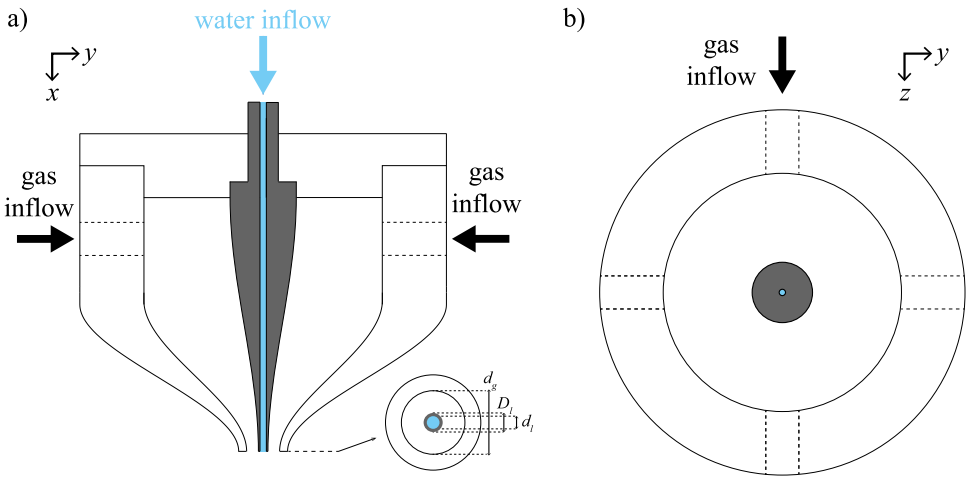

Fig. 1. Nozzle schematic cut longitudinally (left) and transversely (right). Water is injected through a round pipe while gas is injected through four gas ports into a converging nozzle. Note that the inset indicating the exit diameters in (a) has been scaled up by a factor of two for visibility. (For interpretation of the references to color in this figure legend, the reader is referred to the web version of this article.)

Table 1
Simulation's non-dimensional parameters: gas Reynolds number (Re_g), liquid Reynolds number (Re_l), gas-to-liquid dynamic pressure ratio (M), Weber number based on the liquid jet diameter but gas density and slip velocity between the two phases (We), density ratio (ρ^*) and viscosity ratio (μ^*).

$Re_g \equiv \frac{4Q_g}{\sqrt{4\pi A_g}\nu_g}$	$Re_l \equiv \frac{\rho_l U_l d_l}{\mu_l}$	$M \equiv \frac{\rho_g U_g^2}{\rho_l U_l^2}$	$We \equiv \frac{\rho_g (U_g - U_l)^2 d_l}{\sigma}$	$\rho^* \equiv \frac{\rho_l}{\rho_g}$	$\mu^* \equiv \frac{\mu_l}{\mu_g}$
21 400	1200	6.4	39.1	815	65

measurement technique relies on a monochromatic X-ray beam that is sent through the liquid and measured by a receiving pin-diode at 270 kHz. Based on the attenuation of the signal caused by the liquid, the EPL is deduced from Beer–Lambert's Law: $EPL = (1/\mu_a)\ln(I_0/I)$ where I_0 is the incident beam intensity, I is the beam intensity after passing through the spray, and μ_a is the X-ray attenuation coefficient of water at the X-ray wavelength. These point measurements can be raster-scanned across the spray to gather longitudinal or transverse profiles of the liquid depth. Details of this technique are further described in Heindel (2018), Bothell et al. (2020), and the experimental configurations and liquid phase visualization are detailed in Machicoane et al. (2019).

2.3. Numerical methods

We consider an LES approach to the two-phase, incompressible Navier–Stokes equations

$$\nabla \cdot \tilde{\boldsymbol{u}} = 0, \tag{1}$$

$$\frac{\partial \rho \tilde{\boldsymbol{u}}}{\partial t} + \nabla \cdot (\rho \tilde{\boldsymbol{u}} \tilde{\boldsymbol{u}}) = -\nabla \tilde{p} + \rho \boldsymbol{g} + \nabla \cdot \left(\mu \left[\nabla \tilde{\boldsymbol{u}} + \nabla \tilde{\boldsymbol{u}}^{\mathsf{T}}\right]\right) + \nabla \cdot \boldsymbol{\tau}_{SGS} + \boldsymbol{F}_{ST}, \tag{2}$$

where $\tilde{(\cdot)}$ denotes a spatially filtered (resolved) quantity on the mesh, $\boldsymbol{u}$ is the velocity, p is the pressure, ρ is the density, μ is the dynamic viscosity, $\boldsymbol{g}$ is the gravitational acceleration, $\boldsymbol{\tau}_{SGS}$ is the sub-grid scale (SGS) stress, $\boldsymbol{F}_{ST}$ is the surface tension force and t is time. We also consider the volume fraction transport equation

$$\frac{\partial \tilde{\alpha}}{\partial t} + \tilde{\boldsymbol{u}} \cdot \nabla \tilde{\alpha} = 0, \tag{3}$$

where α is the ratio of liquid volume to cell volume in a computational cell and sub-grid scale effects have been neglected. The fluid properties are weighted based on the liquid volume fraction

$$\rho = (1 - \tilde{\alpha})\rho_g + \tilde{\alpha}\rho_l, \tag{4}$$

$$\mu^{-1} = (1 - \tilde{\alpha})\mu_g^{-1} + \tilde{\alpha}\mu_l^{-1}, \tag{5}$$

where subscripts 'g' and 'l' refer to gas and liquid quantities respectively.

The two-phase Navier–Stokes equations are solved using an in-house, conservative, finite-volume flow solver for low Mach number flows (Desjardins et al., 2008). The solver employs second-order accurate methods in time and space. Away from the interface, the flow solver is discretely kinetic energy conserving. At the interface, local discontinuities degrade the methods and although mass is still discretely conserved and momentum is approximately conserved, kinetic energy conservation is lost. The volume fraction equation is solved with a geometric, semi-Lagrangian Volume-of-Fluid method (Owkes and Desjardins, 2014). Inside each computational cell, the interface is represented locally as a plane using the piece-wise linear interface construction (PLIC) (Rider and Kothe, 1998), with the plane normal calculated using LVIRA (Pilliod and Puckett, 2004). A dynamic Smagorinsky turbulence model (Meneveau et al., 2000) is used to close $\boldsymbol{\tau}_{SGS}$. The surface tension force is calculated through

$$\boldsymbol{F}_{ST} = \sigma(\tilde{\kappa} + \kappa_{SGS})\nabla\tilde{\alpha} \tag{6}$$

where σ is the surface tension coefficient, $\tilde{\kappa}$ is the resolved curvature and κ_{SGS} is a sub-grid scale curvature. The surface tension force is embedded as a source term in the pressure Poisson equation using a continuous surface force approach (Popinet and Zaleski, 1999). The resolved curvature of the interface is calculated using parabolic surface fits (Scardovelli and Zaleski, 2003). κ_{SGS} is used to model surface wettability effects that exist at scales far below the mesh size and is controlled through a static contact angle θ_s (see Wang and Desjardins (2018)). Fig. 2 shows a schematic of a grid cell that contains the triple point. In that cell, the mismatch between the interface angle resolved by the mesh (θ_d) and the angle at the wall (θ_s) is used to compute a SGS curvature

$$\kappa_{SGS} = \frac{\cos\theta_s - \cos\theta_d}{\Delta}, \tag{7}$$

where Δ is the mesh spacing. If a cell does not have a triple point, then κ_{SGS} is set to 0.

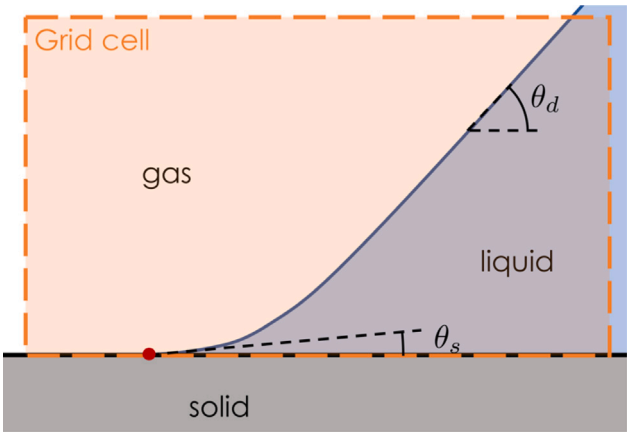

Fig. 2. Schematic of sub-grid scale contact line. The model adds a sub-grid scale curvature based on an assumed static contact angle θ_s to the resolved curvature based on θ_d. (For interpretation of the references to color in this figure legend, the reader is referred to the web version of this article.)

2.4. Simulation set up

2.4.1. Domain

The atomization domain is a rectangular box of size $11.16D_l \times 10D_l \times 10D_l$, discretized on a Cartesian mesh uniformly spaced by $n_x \times n_y \times n_z$ cells. Cells are cubic with sides of length $\Delta/d_l = 0.066$. x is the downstream direction while y and z are the lateral directions with the origin of the domain located at the center of the nozzle exit plane. The liquid is laminar and given a parabolic velocity profile. The gas inflow condition is either specified by a Dirichlet condition according to an analytical profile or a supplementary nozzle simulation. All other boundaries are treated as Neumann outflow conditions.

For some of the atomization simulations presented herein, an auxiliary nozzle simulation of the internal gas flow of the nozzle is used to generate realistic inflow conditions. The domain size of this nozzle simulation is $10d_g \times 10d_g \times 10d_g$ and the mesh is Cartesian with a uniform spacing $\Delta_n/d_g = 0.05$. The gas nozzle simulation is indicated in terms of the gas diameter d_g since it is the relevant quantity here, and we remind that $D_l/d_g = 0.3$. The nozzle plenum is the furthest point upstream in the domain and the furthest point downstream is at a distance d_g past the nozzle exit. The liquid injection is masked out as a solid and a single-phase solver is used, significantly reducing the computational cost. The converging nozzle walls are created by stair-stepping full cells that are treated as solid boundaries and the gas inflow is injected through the four normal ports upstream to match the gas flow rate Q_g. This approach matches the nozzle 3D geometry used in the experiment and available at http://depts.washington.edu/fluidlab/nozzle.shtml. All other boundaries are treated as Neumann outflow conditions. The gas velocity field at $x = -1.16D_l$ is then used as a Dirichlet inflow condition for the atomization simulation.

2.4.2. Range of gas velocity and contact line models

The gas velocity models used in this study were an analytical velocity profile and an additional nozzle simulation of the internal gas flow. The analytical profile Matas et al. (2018) and takes the form

$$\begin{aligned} u(r) &= U_g \mathrm{erf}\big((r-R_l)/\delta_w\big)\big[1+\mathrm{erf}\big((r-R_l)/\delta_w\big)\big]/2 \qquad R_l \le r \le r_g \\ v(r) &= w(r) = 0 \end{aligned} \tag{8}$$

where $R_l = D_l/2$ and $r_g = d_g/2$ are the lower and upper bounds containing the gas stream, r is the radial location, δ_w is the prescribed gas vorticity thickness and U_g is chosen such that the gas volumetric flow rate integrates to Q_g. Fig. 3(a) shows an atomization simulation run with an analytical gas velocity profile while Fig. 3(b) shows a simulation where the nozzle and atomization simulations are coupled as described in Section 2.4.1.

The contact line models used in this study were pinning the contact line to the inner wall ($r = r_l = d_l/2$) pinning to the outer wall ($r = R_l$) and allowing for an unpinned/free moving contact line. The implementation of each is as follows: when pinning to r_l, the splitter plate is modeled as a fully unwet wall while when pinning to R_l, it is modeled as a fully wet wall. In both cases, the splitter plate cells are treated as a solid boundary for the velocity solver, but either taken to be a full liquid or gas cells when included in the LVIRA interface reconstruction. However, in the case where the contact line is free moving, the splitter plate cells are excluded from the LVIRA interface reconstruction but still treated as a solid boundary for velocity. For freely moving contact lines, the SGS contact line model described in Section 2.3 is employed. It should be noted that although the splitter plate is resolved by $2-3$ cells in this study, results presented in the following section show that excellent agreement with experiment is still obtained. More detailed analysis of the contact line in a more highly resolved setting is left for future work.

3. Validation against experiments

The combination of using an additional nozzle simulation to model the gas profile and allowing for a free contact line with a static contact angle of 85° yields the best agreement against experiments; qualitative comparisons are made in Fig. 4 and quantitative comparisons are made against metrics gathered from X-ray measurements in Fig. 5 and from back-lit imaging in Fig. 6. The atomization simulation presented in this section uses a refined mesh of size $\Delta/2$.

Fig. 4 shows snapshots of the flow comparing the simulations and experiments; emphasis is placed on the liquid core. At this low gas-to-liquid dynamic pressure ratio, the main instabilities observed are Kelvin–Helmholtz instabilities that develop just past the nozzle exit and a large-scale flapping instability. At large-scales, both exhibit similar liquid core lengths, interface topology, and flapping motion. The three snapshots illustrate the small-scale event of bag break up. The process begins with the development of a thick sheet, the high-speed gas subsequently inflates this sheet which forms a bag, and finally, when the sheet becomes sufficiently thin, the bag bursts. These thin sheets in the experiment can reach scales as small as $\mathcal{O}(1\ \mu\mathrm{m})$ which computations cannot afford to resolve. In our simulations, the mesh sizes are $\mathcal{O}(100\ \mu\mathrm{m})$ and as such, bags prematurely break and leave behind large rims resembling a prong. Running at these mesh sizes allow simulations to be relatively affordable, costing around 100,000 core hours.

Quantitative comparisons of EPL statistics, liquid core length, and dominant frequency are presented to validate simulations against experiments. EPL is calculated in the simulation by integrating the liquid volume fraction along a line of sight, i.e., $\mathrm{EPL} = \int \alpha dz$. After the flow has reached a statistically stationary state, statistics are accumulated for $T_{stat} = 113 d_l/U_l = 450$ ms, i.e., 113 characteristic liquid time scales, while experimental measurements are gathered for 10 seconds, corresponding to 45 and 1000 flapping events respectively. Fig. 5(a) shows a 2D map of EPL averaged in time. Fig. 5(b) shows the comparison of mean EPL sampled along x, at the centerline ($y = 0$). The mean centerline EPL is a proxy for the liquid diameter at distances close to the nozzle exit and decreases in value downstream either because the flapping instability displaces the liquid core transversely away from the line of sight or the liquid core has deformed or fragmented. EPL measurements presented herein are normalized by D_l since we will later pin the contact line to the outer wall of the liquid pipe, leading to a value of approximately 1 at the nozzle exit, $x/D_l = 0$ (Note: it will not be exactly 1 because of the inexact nature associated with approximating a cylindrical geometry using a Cartesian mesh). Simulations are in excellent agreement with experiments as they are able to match well the centerline decay of mean EPL. Fig. 5(c) shows that the

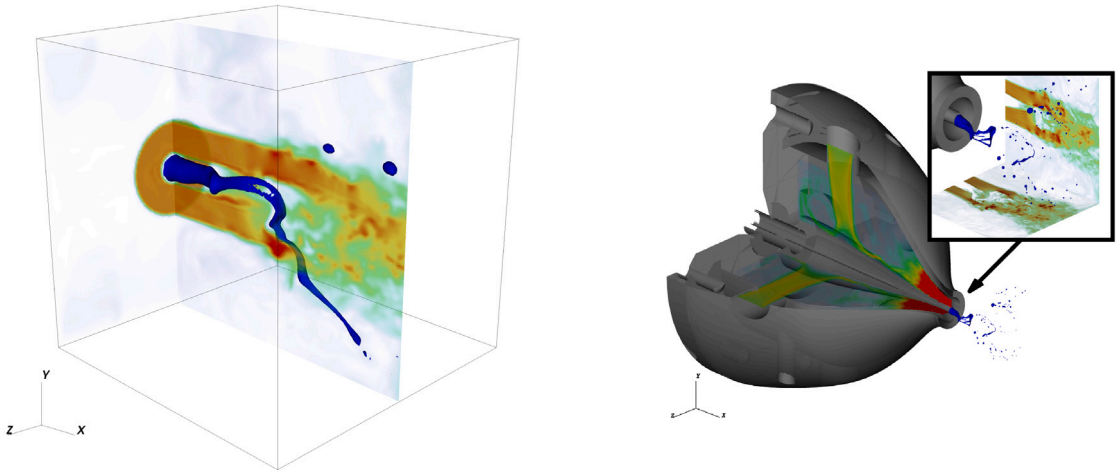

(a) Atomization Domain Only

(b) Atomization and Nozzle Domains Coupled

Fig. 3. Illustration of the computational set up. Contour of $\alpha = 0.5$ representing the interface is plotted in blue, pseudo-color of velocity magnitude are plotted on the cut planes with different normalization inside and outside the nozzle. (a) Domain excludes the nozzle and utilizes an analytical profile to model the gas velocity and (b) a separate nozzle simulation is coupled to the atomization domain. (For interpretation of the references to color in this figure legend, the reader is referred to the web version of this article.)

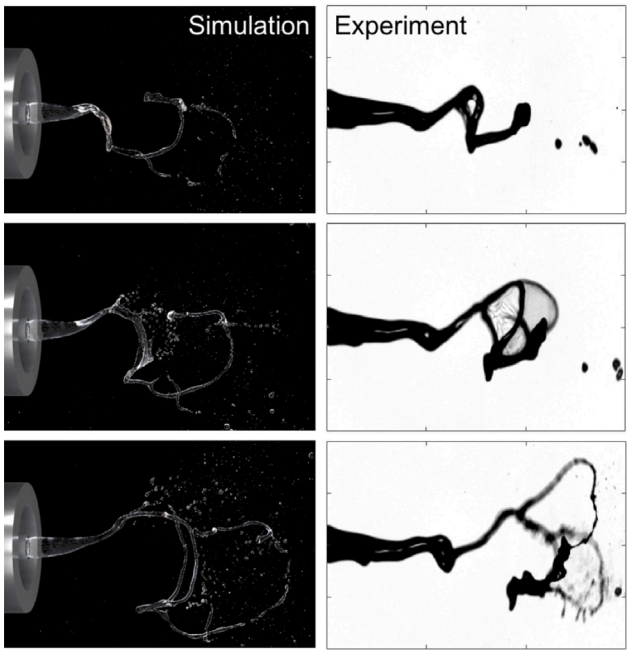

Fig. 4. Qualitative comparisons between the simulation (left) and experiment (right). Frames are separated by 1 ms. (For interpretation of the references to color in this figure legend, the reader is referred to the web version of this article.)

simulations also match well the experimental standard deviation (std) of centerline EPL. Peaks in the standard deviation of EPL occur where variations in the integrated volume fraction over time are largest and in the case of the centerline EPL, are visually confirmed to be a result of large-scale flapping motion. Figs. 5(d) to 5(k) show excellent agreement in transverse EPL mean and standard deviation profiles. Figs. 5(d) to 5(g) show that the simulations matches the transverse mean profiles well, capturing the spreading of the liquid jet. Fig. 5(h) shows two peaks in the standard deviation transverse profile at the top and bottom edges of the jet and can be explained by the variation in volume fraction caused by interfacial perturbations generated by Kelvin–Helmholtz instabilities (Marmottant and Villermaux, 2004; Ricard et al., 2021). Figs. 5(i) to 5(k) show that as the downstream distance is increased, the

Table 2
Comparisons between the simulation and the experiment of mean and standard deviation of L_B and flapping Strouhal number obtained from binarized images.

	$\langle L_B \rangle / D_l$	$L_{B,std} / D_l$	St
Simulation	5.24	1.15	7.52×10^{-3}
Experiment	4.67	0.937	6.63×10^{-3}
Normalized difference	12%	22%	13%

centerline value and the two off-center peaks also increase, indicating a transition from a surface Kelvin–Helmholtz instability to a large-scale flapping instability.

Fig. 6(a) shows a time instance of a binarized image of the liquid core and mimics an experimental back-lit image. The quantities illustrated on the figure are the liquid core length L_B, defined to be the instantaneous longitudinal extent of the liquid core, and the y liquid presence barycenter (y_{bary}) at a downstream location. Fig. 6(b) shows that the simulations agree well with experimental results for the normalized probability density functions (PDF) of L_B. Fig. 6(c) shows a spectrum of a Fourier transform taken of a time signal of y_{bary} (see Kaczmarek et al. (2022) for more details). A flapping Strouhal number is calculated through $St = f_{dom} d_l / U_g$ where f_{dom} is the dominant frequency taken to be the frequency at which the spectrum peaks. y_{bary} $x/D_l = 3$, x/D_l (Delon et al., 2018). Note that this normalization does not claim any physical scaling but is done for non-dimensionalization purposes. Table 2 summarizes the comparison of the mean and standard deviation of L_B and the flapping Strouhal number between the simulations and the experiments.

We now look at the effect of mesh resolution on the statistics presented above. Two additional simulations using larger mesh resolutions Δ and 2Δ are presented. Fig. 7 shows the mean and standard deviation centerline EPL statistics and the PDF of liquid core length at these different mesh sizes. Mean and standard deviation centerline EPL statistics indicate that a simulation with a mesh resolution Δ is relatively well converged because differences between Δ and $\Delta/2$ are small compared to differences between 2Δ and Δ. Furthermore, Fig. 7(c) shows that the liquid core length is not strongly affected by the mesh size. Although discrepancies are still present in statistics between mesh sizes Δ and $\Delta/2$, we conclude that a mesh size Δ is sufficient to draw inferences from. As such, to reduce computational resources, future simulations presented will maintain a mesh size of Δ.

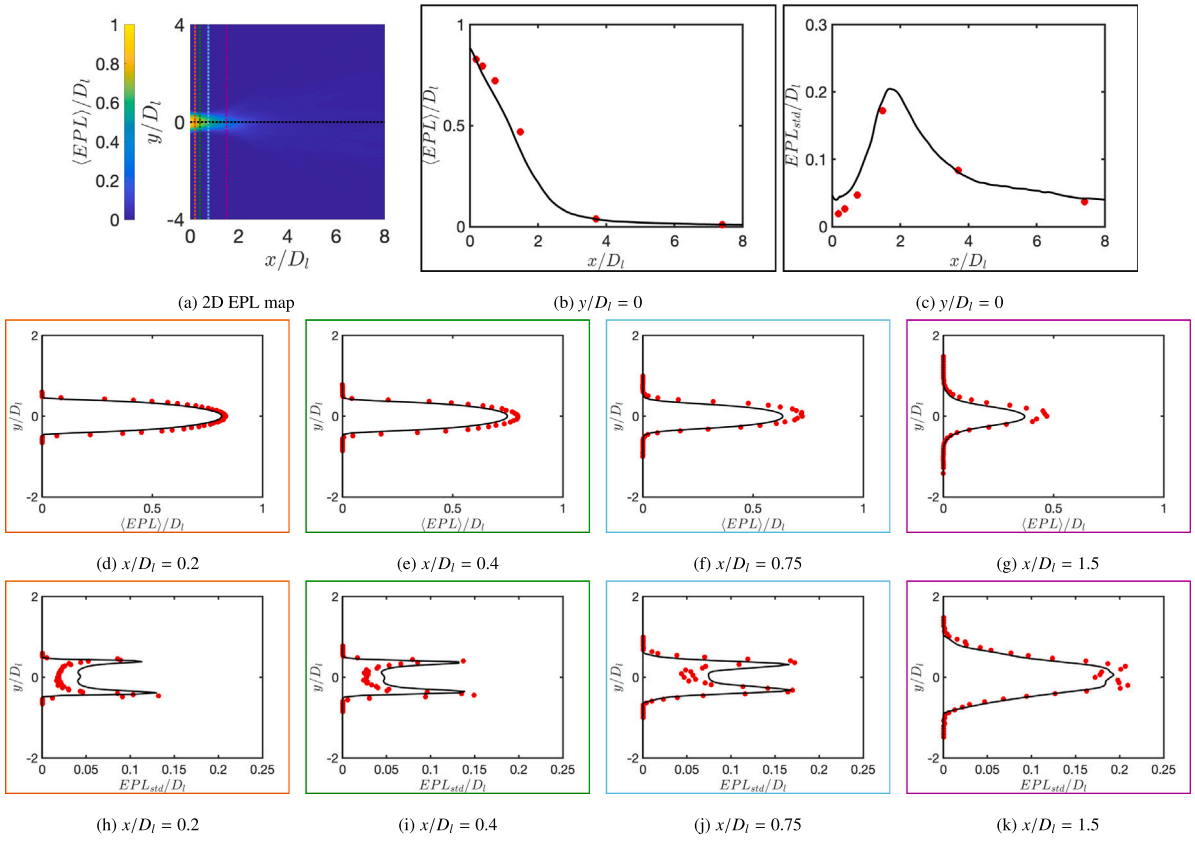

(a) 2D EPL map (b) $y/D_l = 0$ (c) $y/D_l = 0$

(d) $x/D_l = 0.2$ (e) $x/D_l = 0.4$ (f) $x/D_l = 0.75$ (g) $x/D_l = 1.5$

(h) $x/D_l = 0.2$ (i) $x/D_l = 0.4$ (j) $x/D_l = 0.75$ (k) $x/D_l = 1.5$

Fig. 5. Simulations compared against experiments. (a) 2D mean EPL map with sampling locations marked, (b-k) Transverse profiles of the mean (middle row) and standard deviation (bottom row) EPL, comparing the simulation (—) and the experimental measurements (●). (For interpretation of the references to color in this figure legend, the reader is referred to the web version of this article.)

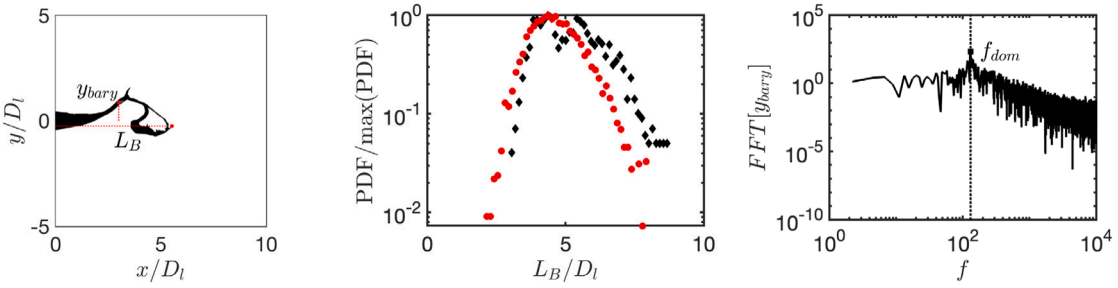

(a) (b) (c)

Fig. 6. (a) Simulation binarized image of the liquid core with relevant quantities, (b) PDF of liquid core length comparing the simulation (♦) and the experiment (●), and (c) y $x/D_l = 3$, f_{dom}.. (For interpretation of the references to color in this figure legend, the reader is referred to the web version of this article.)

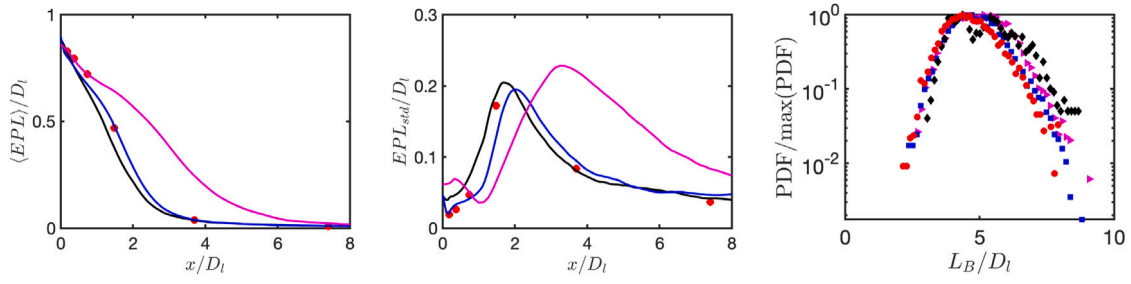

(a) $y/D_l = 0$ (b) $y/D_l = 0$ (c)

Fig. 7. Mesh convergence of (a-b) EPL statistics and (c) liquid core length PDFs for simulations with mesh sizes 2Δ (—, ▶), Δ (—, ■), $\Delta/2$ (—, ♦) compared against experiment (●). (For interpretation of the references to color in this figure legend, the reader is referred to the web version of this article.)

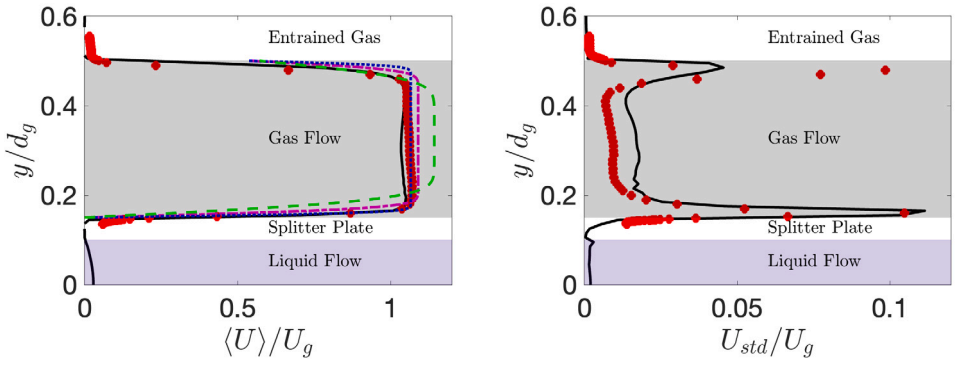

Fig. 8. Comparisons of velocity statistics between analytical profiles with vorticity thicknesses $2\delta_w$ ( ), δ_w ( ), $\delta_w/2$ ( ), additional nozzle simulation ( ) and experiment ( ). Note that $D_l/d_g = 0.3$. (For interpretation of the references to color in this figure legend, the reader is referred to the web version of this article.)

4. Impact of gas velocity model

4.1. Gas velocity profiles

Fig. 8 shows velocity profiles at the nozzle exit plane for the experiment, the auxiliary nozzle simulation and the analytical velocity profiles according to Eq. (8) at different vorticity thicknesses. For the analytical profiles, the vorticity thicknesses used are $2\delta_w$, δ_w and $\delta_w/2$ where $\delta_w = 5.6h/\sqrt{Re_h}$ is the vorticity thickness obtained from the correlation proposed by Marmottant and Villermaux (2004), $h = (D_l - d_g)/2$ and $Re_h = U_g h/\nu_g$. No turbulent fluctuations are added to the inflow velocity profile. The experimental gas velocity profiles were measured a small distance downstream of the nozzle using hot-wires without any liquid present while the statistics in the simulation were sampled in the atomization domain. Various mesh sizes of the auxiliary nozzle simulation were tested and minimal changes in the stream-wise velocity statistics were observed. Fig. 8(a) shows that the mean stream-wise velocity profile of the nozzle simulation and the analytical velocity profile with $\delta_w/2$ match the experimental vorticity thickness at the inner wall while the velocity profiles with vorticity thicknesses of δ_w and $2\delta_w$ are a worse match. Fig. 8(b) shows that the stream-wise standard deviation velocity predicted from the nozzle simulation match the experiment well at the inner wall, which can be expected to be most relevant for atomization, but are under-predicted within the outer gas shear layer.

4.2. Influence of vorticity thickness

Figs. 9(a) and 9(b) show the mean and standard deviation centerline EPL and Fig. 9(c) shows the liquid core length PDF of simulations using an analytical velocity profile at three different gas vorticity thicknesses (i.e., $2\delta_w$, δ_w and $\delta_w/2$). The contact line model used in these simulations was a free contact line with a static contact angle 85°. The simulation presented in Section 3 using a mesh size $\Delta/2$ will serve as a benchmark. Considering the simulation using a gas vorticity thickness δ_w, the mean centerline EPL profile and liquid core length PDF have larger values compared to the benchmark case, suggesting that the jet breaks further downstream than in that case. Reducing the vorticity thickness by a factor of 2 more closely matches the vorticity thickness produced from the nozzle simulation used in the benchmark case and therefore, we observe better agreement in the mean centerline EPL profile. However, discrepancies still remain as the standard deviation centerline EPL for $x/D_l > 3$ and the liquid core length PDF exhibits larger values. This can likely be attributed to the turbulence coming from the nozzle which is known to have a destabilizing effect (Jiang and Ling, 2021) and absent in the analytical inflow velocity profiles. Mean centerline EPL statistics and liquid core length for $2\delta_w$ have much larger values than all cases, confirming that increasing vorticity thickness increases the liquid core length. Table 3 summarizes the mean and standard deviation liquid core length and the flapping Strouhal number. Results show that decreasing the vorticity thickness decreases the mean liquid core length while increasing the dominant frequency. The latter is a trend consistent with past studies (Fuster et al., 2013; Matas et al., 2018) and related to studying the influence of gas velocity deficits on temporal dynamics (Matas et al., 2018, 2011). However, using an analytical profile seems to under-predict the flapping Strouhal number by approximately 30% under the range of vorticity thicknesses presented here. This is further evidence that turbulent fluctuations play a key role on the break up processes and in particular, on the dominant frequencies (Jiang and Ling, 2021; Matas et al., 2015).

Table 3
Summary of mean and standard deviation of L_B and flapping Strouhal number obtained from binarized images for gas velocity profiles at different vorticity thicknesses.

	$\langle L_B \rangle / D_l$	$L_{B,std}/D_l$	St
$2\delta_w$	8.59	0.539	4.66×10^{-3}
δ_w	6.92	1.18	4.93×10^{-3}
$\delta_w/2$	6.24	1.16	5.57×10^{-3}
Benchmark	5.24	1.15	7.52×10^{-3}

5. Impact of contact line model

5.1. Effect of contact line location

The contact line model was varied by pinning the contact line to the splitter plate inner wall, outer wall and allowing for a free moving contact line with a static contact angle of 85°. The gas flow model was maintained as an analytical velocity profile according to Eq. (8) with a vorticity thickness δ_w.

Pinning the interface to the inner wall models the splitter plate as a fully unwet wall. This contact line model creates a gas re-circulation and low pressure region just downstream of the splitter plate. This gives rise to aspiration of the interface in the radial direction towards the gas. The consequence of this is observed in Fig. 10(a) where the initial mean EPL increases as the downstream distance is increased. It is only after $x/D_l \approx 0.25$, that the interface reaches the bulk of the high-speed gas stream and subsequently exhibits a monotonic decrease in mean EPL.

Pinning the interface to the outer wall models the splitter plate as a fully wet wall. Experimental high-resolution visible light imaging and X-ray imaging have shown that at this operating condition, the contact line lies mostly near the outer wall (Heindel, 2018; Ricard et al., 2021). Moreover, when adding swirl to the gas, it is observed that the contact

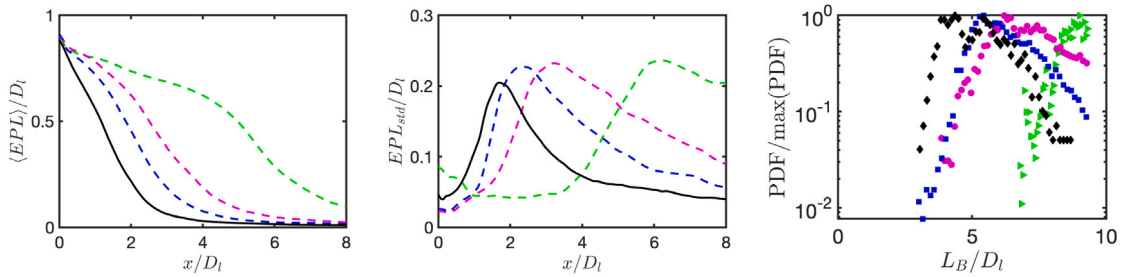

(a) $y/D_l = 0$ (b) $y/D_l = 0$ (c)

Fig. 9. Influence of velocity model on (a-b) EPL statistics and (c) $2\delta_w$ (,), δ_w (,) and $\delta_w/2$ (,) compared against the benchmark (,). (For interpretation of the references to color in this figure legend, the reader is referred to the web version of this article.)

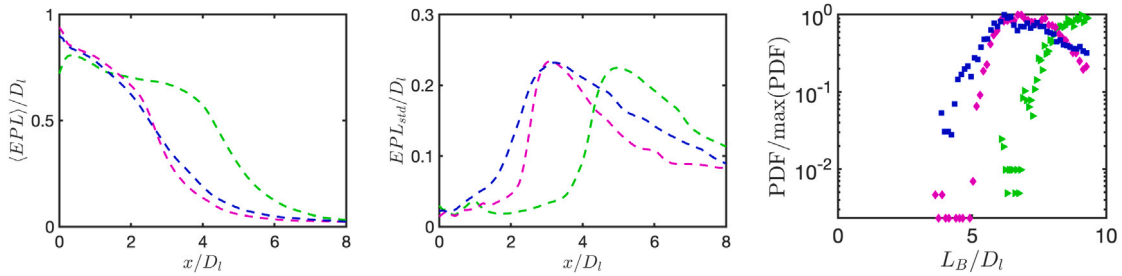

(a) $y/D_l = 0$ (b) $y/D_l = 0$ (c)

Fig. 10. Influence of contact line model on (a-b) EPL statistics and (c) liquid core length PDFs for pinned to inner wall (,), outer wall (,) and a free contact line (,). (For interpretation of the references to color in this figure legend, the reader is referred to the web version of this article.)

line can even wick up into the gas flow region as shown in Fig. 11(a). Therefore, pinning to the outer wall more closely matches the local experimental flow configuration. This pinning model results in a mean centerline EPL that decreases monotonically which is experimentally observed (see Fig. 5(b)).

One can see in Fig. 10(a) that using a free contact line with an SGS contact line force with $\theta_s = 85°$ leads to similar mean EPL profiles to pinning to the outer wall. Fig. 11(b) shows the PDF of the normalized radial location for the contact line such that a value of 0 indicates the interface is located at the inner wall while a value of 1 indicates it is at the outer wall. For $\theta_s = 85°$, the contact line radius peaks near the outer wall, serving as an explanation of why pinning to the outer wall and this free contact line have similar mean EPL profiles. It can be observed in Fig. 10(b) that a free contact line model leads to more interfacial dynamics than pinning the outer wall since its standard deviation EPL profile is uniformly larger.

Fig. 10(c) shows the PDF of the liquid core length and Table 4 summarizes the mean and standard deviation centerline EPL and Strouhal numbers for all three cases. Pinning to the inner wall leads to a liquid that is too stable as quantified by the large mean liquid core length and at times, the liquid core length is observed to exceed the downstream domain boundary. Pinning to the outer wall and having a free contact line have similar PDFs, with the free contact line exhibiting a slightly smaller mean liquid core length. Studies have shown that the vorticity thickness has a strong impact on the dominant frequency (Fuster et al., 2013; Matas et al., 2018). Results show that the flapping Strouhal numbers are all within 2% of each other, suggesting that the dominant frequency is mostly independent of the contact line model for a fixed vorticity thickness.

Table 4
Summary of mean and standard deviation of L_B and flapping Strouhal number for different contact line models.

	$\langle L_B \rangle / D_l$	$L_{B,std}/D_l$	St
Pin to inner wall	8.50	0.583	4.92×10^{-3}
Pin to outer wall	7.16	0.950	5.06×10^{-3}
Free contact line	6.92	1.18	4.92×10^{-3}

5.2. Effect of static contact angle θ_s

The static contact angle depends on many factors such as surface roughness, temperature, nozzle material and treatment. For aluminum, water and air, a reasonable static contact angle is between 70°–90° (Zhu et al., 2012; Majeed, 2014). In the present study, we consider the static contact angles 70°, 85°, and 110° which model a moderately hydrophilic, less hydrophilic, and moderately hydrophobic surface respectively. In these simulations, an auxiliary nozzle simulation was used to provide the gas inflow velocity. Fig. 11(b) shows the contact line radius PDFs measured at a fixed arc location. The PDFs show that the contact lines sit very close to the outer wall for $\theta_s = 70°$, further away from the outer wall for $\theta_s = 85°$ and near the inner wall for $\theta_s = 110°$. Fig. 12(a) shows the mean and standard deviation centerline EPL profiles for simulations using these static contact angles. Because a simulation using $\theta_s = 110°$ results in a contact line close to the inner wall, its EPL profile follows a similar behavior to pinning to the inner wall, with an initial increase in EPL and subsequent monotonic decrease. Similarly, a simulation using $\theta_s = 70°$ results in a contact line close to the outer wall and as such, exhibits a behavior similar to pinning to the outer wall in that a monotonic decrease in EPL is observed. Fig. 12(b) shows that increasing θ_s shifts the standard deviation centerline EPL to the right. Fig. 12(c) shows the PDFs of the liquid core length for simulations using $\theta_s = 70°$ and 85° are similar while 110° results in a profile shifted to the right. Table 5 summarizes the mean and standard deviation centerline EPL and flapping Strouhal number showing that as θ_s is increased, the liquid core length and dominant frequency also increase. This highlights the significant impact that the contact angle model can have on the downstream liquid distribution.

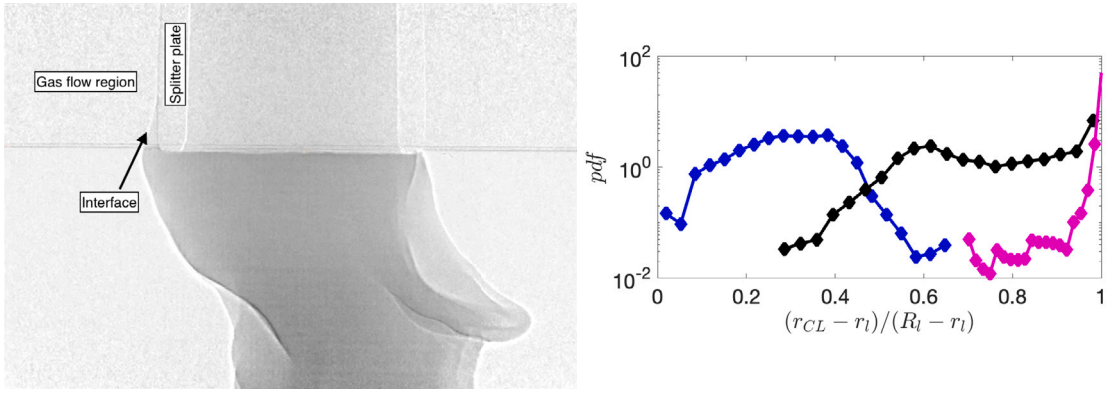

(a) Experimental Image (b) PDF of contact line radius

Fig. 11. (a) Experimental image showing an instance where the contact line wicked up the outer wall into the gas flow region in the presence of gas swirl and (b) $\theta_s = 70°$ (—), $\theta_s = 85°$ (—), $\theta_s = 110°$ (—). (For interpretation of the references to color in this figure legend, the reader is referred to the web version of this article.)

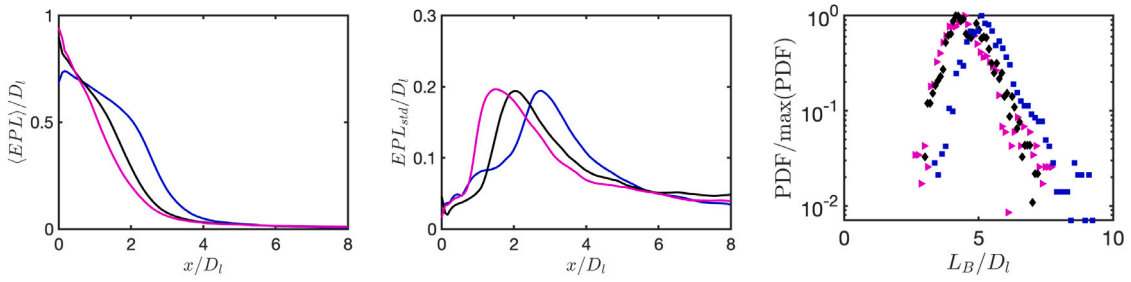

(a) $y/D_l = 0$ (b) $y/D_l = 0$ (c)

Fig. 12. Influence of static contact angle on (a-b) EPL statistics and (c) liquid core length PDFs for $\theta_s = 70°$ (—, ▶), 85° (—, ♦), and 110° (—, ■). (For interpretation of the references to color in this figure legend, the reader is referred to the web version of this article.)

Table 5
Summary of mean and standard deviation of L_B and flapping Strouhal number for different static contact angles.

θ_s	$\langle L_B \rangle / D_l$	$L_{B,std}/D_l$	St
70°	4.52	0.810	7.01×10^{-3}
85°	4.65	0.751	6.63×10^{-3}
110°	5.38	0.866	8.56×10^{-3}

6. Conclusion

In this study, we have performed simulations of air-blast atomization in a coaxial two-fluid atomizer using a geometric Volume-of-Fluid method. Simulations were validated against experiments under identical air/water conditions and geometries. Excellent agreement of quantities such as the mean equivalent path length of the liquid (EPL), liquid core length, and dominant frequency was observed. A mesh refinement study was also conducted showing that these quantities were reasonably well mesh converged. The liquid was modeled using a Poiseuille flow while the gas inflow and contact line models were studied.

The gas inflow models considered were analytical velocity profiles at different vorticity thicknesses with no turbulent fluctuations added and an auxiliary nozzle simulation. Simulations using analytical velocity profiles were benchmarked against a simulation using the nozzle simulation. Results showed that decreasing the vorticity thickness decreased the mean liquid core length, the mean centerline EPL, and increased the dominant frequency of the liquid jet motions. While one analytical profile had a vorticity thickness that was close in value to the experiment and nozzle simulation, quantities such as the mean liquid core length remained larger. Furthermore, although decreasing the vorticity thickness increased the dominant frequency, a trend reported in other studies (Fuster et al., 2013; Matas et al., 2018), the dominant frequencies for the presented vorticity thicknesses yielded systematically lower values than the experiment. These results confirmed that turbulent fluctuations in the gas play an important role.

The contact line models considered were pinning to the inner wall of the splitter plate, the outer wall of the splitter plate, and allowing for a free contact line with a (SGS) contact line model using a static contact angle of 85°. This study showed that the contact line model has a key influence on the liquid jet development and on the liquid distribution downstream. In particular, pinning to the outer wall or using a free moving contact line yielded better experimental agreement of quantities such as mean and standard deviation centerline EPL and mean liquid core length than pinning to the inner wall. Pinning to the inner wall resulted in an initial increase in mean centerline EPL downstream of the nozzle because of a re-circulation region created by the gas. In contrast, pinning to the outer wall or having a free moving contact line resulted in the monotonic decrease in EPL observed in the experiment. Results also indicated that when using an analytical gas velocity profile with a fixed vorticity thickness, the contact line model does not have a significant impact on the dominant frequency. The static contact angle was varied between $\theta_s = 70°$, $\theta_s = 85°$, and $\theta_s = 110°$. Results showed in the $\theta_s = 70°$ case, i.e., modeling a hydrophylic surface, the mean centerline EPL exhibited similar trends to pinning to the outer wall while in the $\theta_s = 110°$ case, i.e., modeling a hydrophobic surface, trends were similar to pinning to the inner wall.

As the near-field region has been validated in this study and a better understanding of the impact of the gas velocity and contact line models have been gained, several research questions remain open. Since computational tools now result in strong agreement of liquid distribution

compared against experiment, our research efforts will now shift to modeling the conversion of broken liquid structures in atomization simulations to Lagrangian particles in spray dispersion simulations. Promising research efforts have been made in this direction (e.g., Kim and Moin (2010), Tomar et al. (2010)) (Chiodi and Desjardins, 2022). The inflow modeling of the gas has been studied in various forms which include modeling the velocity profile just downstream of the nozzle exit using a velocity deficit (e.g., Matas et al. (2018, 2011)). However, current literature has not considered in detail the influence of the contact line which this study has shown to have an impact. Thus, a more detailed study of the contact line physics and different modeling strategies for the contact line would be useful.

Declaration of competing interest

The authors declare that they have no known competing financial interests or personal relationships that could have appeared to influence the work reported in this paper.

Data availability

Data will be made available on request.

Acknowledgments

This work was sponsored by the Office of Naval Research (ONR), USA as part of the Multidisciplinary University Research Initiatives (MURI) Program, under grant number N00014-16-1-2617. The views and conclusions contained herein are those of the authors only and should not be interpreted as representing those of ONR, the U.S. Navy or the U.S. Government.

The X-ray imaging work was performed at the 7-BM beamline of the Advanced Photon Source, a U.S. Department of Energy (DOE) Office of Science User Facility operated for the DOE Office of Science by Argonne National Laboratory under Contract No. DE-AC02-06CH11357.

References

Agbaglah, G., Chiodi, R., Desjardins, O., 2017. Numerical simulation of the initial destabilization of an air-blasted liquid layer. J. Fluid Mech. 812, 1024–1038.

Anderson, D.M., McFadden, G.B., Wheeler, A.A., 1998. Diffuse-interface methods in fluid mechanics. Annu. Rev. Fluid Mech. 30 (1), 139–165.

Bothell, J.K., Machicoane, N., Li, D., Morgan, T.B., Aliseda, A., Kastengren, A.L., Heindel, T.J., 2020. Comparison of X-ray and optical measurements in the near-field of an optically dense coaxial air-assisted atomizer. Int. J. Multiph. Flow. 125, 103219.

Carmona, J., Odier, N., Desjardins, O., Cuenot, B., Misdariis, A., Cayre, A., 2021. A comparative study of direct numerical simulation and experimental results on a prefilming airblast atomization configuration. At. Sprays 31 (8), 9–32.

Chiodi, R., Desjardins, O., 2017. A reformulation of the conservative level set reinitialization equation for accurate and robust simulation of complex multiphase flows. J. Comput. Phys. 343, 186–200.

Chiodi, R., Desjardins, O., 2022. General, robust, and efficient polyhedron intersection in the interface reconstruction library. J. Comput. Phys. 449, 110787.

Delon, A., Cartellier, A., Matas, J.P., 2018. Flapping instability of a liquid jet. Phys. Rev. Fluids 3, 043901.

Demoulin, F., Beau, P., Blokkeel, G., Mura, A., Borghi, R., 2007. A new model for turbulent flows with large density fluctuations: Application to liquid atomization. At. Sprays 17, 315–345.

Desjardins, O., Blanquart, G., Balarac, G., Pitsch, H., 2008. High order conservative finite difference scheme for variable density low Mach number turbulent flows. J. Comput. Phys. 227, 7125–7159.

Fuster, D., Bagué, A., Boeck, T., Le Moyne, L., Leboissetier, A., Popinet, S., Ray, P., Scardovelli, R., Zaleski, S., 2009. Simulation of primary atomization with an octree adaptive mesh refinement and VOF method. Int. J. Multiph. Flow. 35, 550–565.

Fuster, D., Matas, J.P., Marty, S., Popinet, S., Hoepffner, J., Cartellier, A., Zaleski, S., 2013. Instability regimes in the primary breakup region of planar coflowing sheets. J. Fluid Mech. 736, 150–176.

Gorokhovski, M., Herrmann, M., 2008. Modeling primary atomization. Annu. Rev. Fluid Mech. 40, 343–366.

Heindel, T.J., 2018. X-Ray imaging techniques to quantify spray characteristics in the near-field. At. Sprays 28, 1029–1059.

Hermann, M., 2008. A balanced force refined level set grid method for two-phase flows on unstructured flow solver grids. J. Comput. Phys. 227, 2674–2706.

Jiang, D., Ling, Y., 2021. Impact of inlet gas turbulence on the formation, development and breakup of interfacial waves in a two-phase mixing layer. J. Fluid Mech. 921, A15.

Kaczmarek, M., Osuna-Orozco, R., Huck, P., Aliseda, A., Machicoane, N., 2022. Spatial characterization of the flapping instability of a laminar liquid jet fragmented by a swirled gas co-flow. Int. J. Multiph. Flow. 152, 104056.

Kastengren, A., Powell, C.F., Arms, D., Dufresne, E.M., Gibson, H., Wang, J., 2012. The 7BM beamline at the APS: A facility for time-resolved fluid dynamics measurements. J. Synchrotron Radiat. 19 (4), 654–657.

Kim, D., Moin, P., 2010. Subgrid-scale capillary breakup model for liquid jet atomization. Combust. Sci. Technol. 192, 1334–1357.

Ling, Y., Fuster, D., Zaleski, S., Tryggvason, G., 2017. Spray formation in a quasi-planar gas-liquid mixing layer at moderate density ratios: A numerical closeup. Phys. Rev. Fluids 2, 014005.

Machicoane, N., Bothell, J.K., Li, D., Morgan, T.B., Heindel, T.J., Kastengren, A.L., Aliseda, A., 2019. Synchrotron radiography characterization of the liquid core dynamics in a canonical two-fluid coaxial atomizer. Int. J. Multiph. Flow. 115, 1–8.

Machicoane, N., Ricard, G., Osuna-Orozco, R., Huck, P., Aliseda, A., 2020. Influence of steady and oscillating swirl on the near-field spray characteristics in a two-fluid coaxial atomizer. Int. J. Multiph. Flow. 129, 103318.

Majeed, M.H., 2014. Static contact angle and large water droplet thickness measurements with the change of water temperature. Al-Nahrain J. Eng. Sci. 17, 114–128.

Marmottant, P., Villermaux, E., 2004. On spray formation. J. Fluid Mech. 498, 73–111.

Matas, J.P., Delon, A., Cartellier, A., 2018. Shear instability of an axisymmetric air–water coaxial jet. J. Fluid Mech. 843, 575–600.

Matas, J.P., Marty, S., Cartellier, A., 2011. Experimental and analytical study of the shear instability of a gas-liquid mixing layer. Phys. Fluids 23 (9), 094112.

Matas, J.P., Marty, S., Dem, M.S., Cartellier, A., 2015. Influence of gas turbulence on the instability of an air-water mixing layer. Phys. Rev. Lett. 115, 074501.

Meneveau, C., Lund, T.S., Cabot, W.H., 2000. A Lagrangian dynamic subgrid-scale model of turbulence. J. Fluid Mech. 319, 353–385.

Müller, T., Sänger, A., Habisreuther, P., Jakobs, T., Trimis, D., Kolb, T., Zarzalis, N., 2016. Simulation of the primary breakup of a high-viscosity liquid jet by a coaxial annular gas flow. Int. J. Multiph. Flow. 87, 212–228.

Owkes, M., Desjardins, O., 2014. A computational framework for conservative, three-dimensional, unsplit, geometric transport with application to the volume-of-fluid (VOF) method. J. Comput. Phys. 270, 587–612.

Pilliod, J.E., Puckett, E.G., 2004. Second-order accurate volume-of-fluid algorithms for tracking material interfaces. J. Comput. Phys. 199, 465–502.

Popinet, S., Zaleski, S., 1999. A front-tracking algorithm for accurate representation of surface tension. Internat. J. Numer. Methods Fluids 30, 775–793.

Ricard, G., Machicoane, N., Osuna-Orozco, R., Huck, P.D., Aliseda, A., 2021. Role of convective acceleration in the interfacial instability of liquid-gas coaxial jets. Phys. Rev. Fluids 6, 084302.

Rider, W.J., Kothe, D.B., 1998. Reconstructing volume tracking. J. Comput. Phys. 141 (2), 112–152.

Scardovelli, R., Zaleski, S., 2003. Interface reconstruction with least-square fit and split Eulerian–Lagrangian advection. Internat. J. Numer. Methods Fluids 41.

Sethian, J.A., Smereka, P., 2003. Level set methods for fluid interfaces. Annu. Rev. Fluid Mech. 35 (1), 341–372.

Tomar, G., Fuster, D., Zaleski, S., Popinet, S., 2010. Multiscale simulations of primary atomization. Comput. & Fluids 39, 1864–1874.

Tryggvason, G., Bunner, B., Esmaeeli, A., Juric, D., Al-Rawahi, N., et al., 2001. A front-tracking method for the computations of multiphase flow. J. Comput. Phys. 169 (2), 708–759.

Wang, S., Desjardins, O., 2018. 3D numerical study of large-scale two-phase flows with contact lines and application to drop detachment from a horizontal fiber. Int. J. Multiphase Flows 101, 35–46.

Xiao, F., Dianat, M., McGuirk, J.J., 2014. LES of turbulent liquid jet primary breakup in turbulent coaxial air flow. Int. J. Multiph. Flow. 60, 103–118.

Zhu, Z.Q., Wang, Y., Liu, Q., Xie, J., 2012. Influence of bond number on behaviors of liquid drops deposited onto solid substrates. Microgravity Sci. Technol. 24.